Progress status for the Mu2e calorimeter system

2015 J. Phys.: Conf. Ser. 587 012047

(http://iopscience.iop.org/1742-6596/587/1/012047)

Journal of Physics: Conference Series **587** (2015) 012047 doi:10.1088/1742-6596/587/1/012047

Progress status for the Mu2e calorimeter system

Gianantonio Pezzullo[1,2], J. Budagov[3], R. Carosi[2], F. Cervelli[1,2], C. Cheng[4], M. Cordelli[5], G. Corradi[5], Yu. Davydov[3], B. Echenard[4], S. Giovannella[5], V. Glagolev[3], F. Happacher[5], D. Hitlin[4], A.Luca[5], M.Martini[4], S. Miscetti[5], P. Murat[7], P. Ongmonkolkul[4], F. Porter[4], A. Saputi[5], I. Sarra[5], F. Spinella[2],V.Stomaci[5], G. Tassielli[6]

[a]Departement of Physics, University of Pisa, Largo B. Pontecorvo 3, Pisa , Italy
[b] INFN sezione di Pisa, Italy, Largo B. Pontecorvo 3, Pisa , Italy
[c] Joint Institute for Nuclear Research, Joliot-Curie 6, Dubna, Russia
[d] Departement of Physics, California Institute of Technology, 1200 E California Blvd, Pasadena (CA), USA
[e] INFN Laboratori Nazionali di Frascati, via Enrico Femri 40, Frascati, Italy
[g] INFN sezione di Lecce, Via Arnesano 73100, Lecce, Italy
[h] Fermi National Accelerator Laboratory, Main Entrance Rd, Batavia (IL), USA

E-mail: pezzullo@pi.infn.it

Abstract. The Mu2e experiment at FNAL aims to measure the charged-lepton flavor violating neutrinoless conversion of a negative muon into an electron. The conversion results in a monochromatic electron with an energy slightly below the muon rest mass (104.97 MeV). The calorimeter should confirm that the candidates reconstructed by the extremely precise tracker system are indeed conversion electrons while performing a powerful μ /e particle identification. Moreover, it should also provide a high level trigger for the experiment independently from the tracker system. The calorimeter should also be able to keep functionality in an environment where the background delivers a dose of $\sim$ 10 krad/year in the hottest area and to work in the presence of 1 T axial magnetic field. These requirements translate in the design of a calorimeter with large acceptance, good energy resolution O(5%) and a reasonable position (time) resolution of $\sim$ <1 cm (<0.5ns). The baseline version of the calorimeter is composed by two disks of inner (outer) radius of 351 (660) mm filled by 1860 hexagonal BaF_2 crystals of 20 cm length. Each crystal is readout by two large area APD's. In this paper, we summarize the experimental tests done so far as well as the simulation studies in the Mu2e environment.

1. Introduction

Several experiments of the last decades proved that lepton-flavor-violation (LFV) for neutral leptons (neutrinos) is a fact. This implies that also charged LFV (cLFV) is possible, but with a rate not yet reached by the current experimental sensitivity. An observation of a cLFV signal would be an unambiguous evidence of new physics. A method to search for cLFV exploits muons; so far two processes involving muons have been studied: $\mu \to e\gamma$ and $\mu N \to eN$. The current upper limits for these two processes are: $BR(\mu \to e\gamma) < 5.7 \times 10^{-13}$ [1] and $R_{\mu e}$(Au targets) $< 7\times10^{-13}$ [2]. Compared to $\mu \to e\gamma$, the rate of $\mu N \to eN$ is scaled by a factor of $\sim \alpha Z^2$, as the photon becomes virtual and couples with the nucleus. Due to the interaction with the nucleus, additional new physics processes can contribute to $\mu N \to eN$ compared to $\mu \to e\gamma$, the ones with a contact term or a four-fermion interaction, such as compositeness or

lepto-quarks[3]. The search for muon conversion has a clear signature to look for. Indeed in the muon conversion process the initial state is a muonic atom that makes a transition to a 2-body state consisting of a mono-energetic electron recoiling to the atomic nucleus, with no neutrinos in the final state and no nucleus breakup. The nucleus is not observed while the conversion electron (CE) has an energy of the muon rest mass minus small corrections for the recoil and the binding energy of the muon.

2. The Mu2e experiment set-up

The Mu2e experiment [4] is composed by three main superconducting magnet systems (see figure 1). The first is the production solenoid (PS) where an intense 8 GeV proton beam (pulsed with a period of $\sim$ 1800 ns) strikes a tungsten target producing mostly π 's. A graded magnetic field (from 2.5 to 4.6 T) then collects most of the produced charged particles and moves them through the second magnet, the transport solenoid (TS). The TS is dedicated to move and select

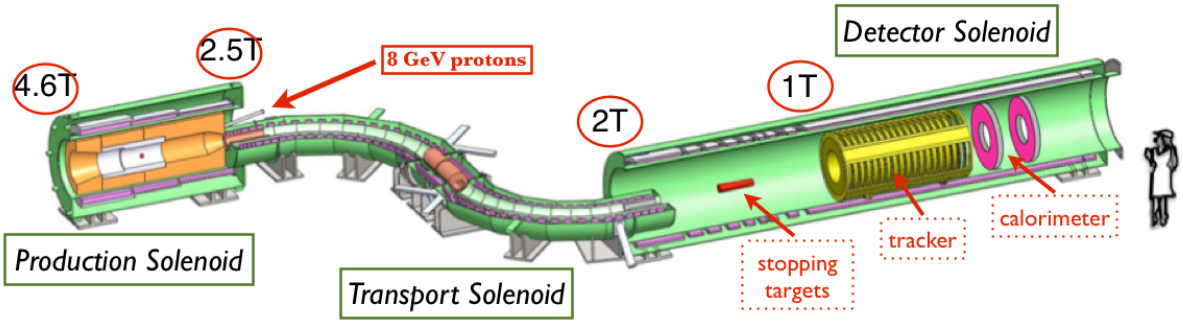

Figure 1. Mu2e experimental layout. The Cosmic ray veto is not shown.

only negative low-momentum muons through the last solenoid, the detector solenoid (DS). Such a selection is done by means of a system of collimators at the sides and in the middle of the TS. The S shape of the transport solenoid allows also to avoid that all neutral particles generated in the PS reach the DS. The DS is the solenoid where the muon beam arrives, stops on the target and the reaction products are analized by the detectors. In order to do that, it houses the muon stopping targets (Al) and the detection system devoted to identify and analyze the conversion electrons (CE). The Al targets reside in a graded field region that varies from 2 to a 1 T, so that electrons emitted upstream are reflected downstream through the detectors region. Downstream the targets a proton absorber, made of high density polyethylene is located to reduce the proton flux (produced in nuclear reactions) to the tracker. The tracking system consists of 20 straw tubes stations designed for maximizing the acceptance and the precise reconstruction of the CE. This is the main detector of the experiment and it is expected to get a resolution of $\sim$ 120 keV/c for 100 MeV/c momentum. The second detector adopted is a crystal electromagnetic calorimeter (EMC) that will be described in details in the next section 3. A Cosmic Ray Veto (CRV) system surrounds the DS on three sides (the ground is not covered) and extends up to the midpoint of the TS; it consists of four layers of extruded scintillator bars with embedded wavelength shifting fibers read out with Silicon photomultipliers (SiPM's). The Veto signal corresponds to coincident hits in three out of four layers. It is designed to reduce the number of expected cosmic induced background events to 0.05 events during the entire running period (three years). In the region of the muon stopping target the CRV is expected to be 99.99% efficient. Neutron shields, made of concrete blocks, are also present between the DS and the

CRV to reduce the neutron flux (coming from the muon stopping targets) which otherwise can compromise the efficiency and functionality of the CRV.

3. The Mu2e Calorimeter

3.1. Calorimeter requirements

The Mu2e calorimeter should confirm that the candidates reconstructed by the extremely precise tracker system are indeed conversion electrons while performing a powerful mu/e particle identification. Moreover, it should provide a high level trigger for the experiment, independently from the tracker system, to bring the rate on disk to $\sim$ few kHz. The calorimeter should also be able to keep functionality in an environment where the background delivers a dose of ~ 12 krad/year in the hottest area and to work in the presence of 1 T axial magnetic field. The calorimeter will also help on selecting correct hits in the tracker. All these requirements translate in the following parameters to be satisfied by the Mu2e calorimeter:

- Provide a large acceptance for electron and positron tracks.
- Determine the energy with a resolution of O(5 MeV).
- Reconstruct the time with a resolution ≤ 0.5 ns.
- Reconstruct the impact position with a resolution better than ~ 1 cm

The calorimeter should survive in the Mu2e environment where a radiation dose of 100 Gy/year/crystal is expected in the hottest areas. Moreover, the calorimeter is embedded in the DS where a 1 T magnetic axial field exists.

3.2. Calorimeter design

The calorimeter design consists of two disks whose dimension have been optimized by simulating signal electron events with the official Mu2e framwork [8]. Simulation results (see table 1) shows that the calorimeter acceptance gets its maximum with an inner (outer) radius of 35.1 (66) cm.

Table 1. Calorimeter configurations studied for optimizing the geometry.

Crystal apothem [cm]	Disk radii [cm]	# crystal	Crystal volume [cm^3]	Efficiency [%]
1.55	35.91/64.3	996	168830	90.5 ± 0.6
1.55	35.91/67.23	1110	193998	90.4 ± 0.6
1.6	34.01/66.35	1044	194424	92.2 ± 0.6
1.6	37.1/66.35	966	179898	90.2 ± 0.6
1.65	35.1/66.0	930	184188	92.2 ± 0.6
1.7	36.12/64.73	798	167769	90.4 ± 0.6

Figure 3 shows that the optimum disks separation is 75 cm, which is $\sim \frac{1}{2}$ wave-length of the signal electron helix.

Each disk is composed by ~ 930 BaF_2 hexagonal crystals, see figure **??**, with a length of 20 cm and a distance among flats of 1.65 cm. The readout system is constitued by two large area APD's, in order to grant a better light yield while providing redundancy of the readout system.

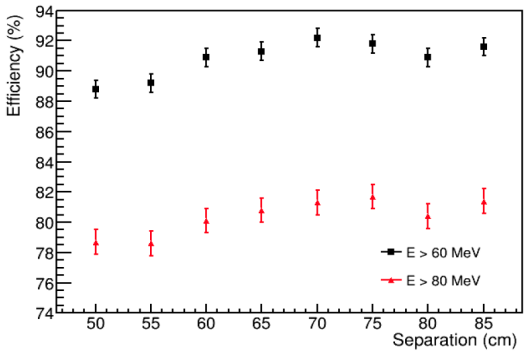

Figure 2. Calorimeter acceptance versus the disk separation.

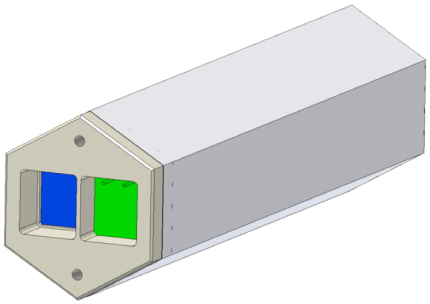

Figure 3. Crystal shape with APD's boxes colored on blue and green.

Table 2. Several configurations studied for optimizing the geoemtry.

Crystal	BaF_2	LYSO	CsI	$PbWO_4$
Density [g/cm^3]	4.89	7.28	4.51	8.28
Radiation length [cm] X_0	2.03	1.14	1.86	0.9
Molieère radius [cm] R_m	3.10	2.07	3.57	2.0
Interaction length [cm]	30.7	20.9	39.3	20.7
dE/dx [MeV/cm]	6.5	10.0	5.56	13.0
Refractive Index at λ_{max}	1.50	1.82	1.95	2.20
Peak luminescence [nm]	220, 300	402	310	420
Decay time τ [ns]	0.9, 650	40	26	30, 10
Light yield (compared to NaI(TI)) [%]	4.1, 3.6	85	3.6	0.3, 0.1
Light yield variation with temperature [%/°C]	0.1, -1.9	-0.2	-1.4	-2.5
Hygroscopicity	None	None	Slight	None

3.3. Crystal choice

In the Conceptual Design Report [4] the calorimeter baseline choice was based on LYSO crystals. Since then, estensive R&D program has been carried out on this option and test beams [5] and electronic design were tuned accordingly. However, during the last year, and despite an active R&D program at Caltech, in cooperation with SICCAS and SIPAT, aiming to reduce the commercial price of LYSO crystals, the large increase in Lu2O3 salt price over the past two years has made the cost of a LYSO calorimeter unaffordable.

Table 2 shows the alternatives which have been studied. At the end, we have selected BaF_2 as baseline choice due to the following advantages:

- it has a small decay time of the fast component;
- it is not hygroscopic;
- It is rad hard.

However BaF_2 presents also some drawbacks and difficulties. In particular, the fast component is emitted in the deep UV region at 220 nm (see figure 5) and, moreover, there is a large component (peaked at 300 nm) that has a long decay time of 650 ns. Name of the game for this crystal is to find an adequate photosensor.

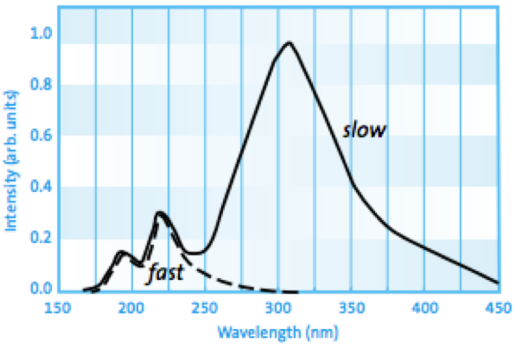

Figure 4. BaF_2 emission spectrum.

3.4. Photosensor choice

There are not existing photosensor candidates for BaF_2 readout that could have a high quantum efficiency at 220 nm while working in the presence of 1 T magnetic field. Photomultipliers are excluded. Channel plate PMTs are at present far too expensive, although spinoffs from the LAPPD project are still being pursued. Our main thrust, however, is to use solid state photosensors, either APD's, SiPMs or MPPCs, with extended UV response. APD's and MPPCs from Hamamatsu and RMD made without the normal protective epoxy coating, and therefore somewhat fragile, can have quantum efficiencies in the 200 nm region of $\sim 17\%$, but do not discriminate between the 220 nm fast component and 300 nm slow component of BaF_2 . The presence of the slow component limits the rate capability of the calorimeter, and can therefore be an issue in high background conditions. We are pursuing an experimental R&D approach to both improving the photosensor quantum efficiency and the slow component discrimination. A Caltech/JPL/RMD consortium has been formed to develop a modified RMD large-area APD into a delta-doped superlattice APD. This device will also incorporate an atomic layer deposition antireflection filter that will provide 60% quantum efficiency at 220 nm and $\sim 0.1\%$ efficiency at 300 nm, thereby enabling us to not only have a larger number of photoelectrons/MeV (x3), but also to take full advantage of the fast decay time component of BaF_2 . The greatly reduced undepleted region of this device will also result in substantially improved rise time of the device.

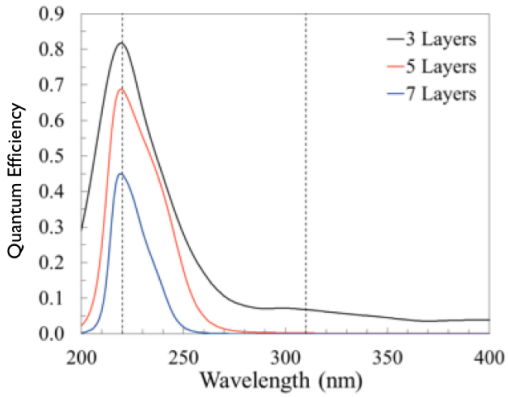

Figure 5. QE versus wavelength of 3 different samples of APD's with different number of atomic layer deposition. The red line rapresent the selected APD.

Conventional RMD APD's will be thinned to remove the surface and undepleted region before

the avalanche layer, and the superlattice structure and optimized antireflection coating will then be deposited at the JPL Microdevices Lab. Figure 5 shows the calculated QE response of the resulting APD as a function of wavelength. For a five-layer AR coating, the QE at the fast component of BaF2 is nearly 70%, and the extinction at the slow component wavelength is nearly complete.

3.5. Energy resolution

The study of the expected energy resolution has been factorized in two steps:

(i) Estimate of the light yield via measurements done in laboratory;

(ii) Simulation of the calorimeter performance in the Mu2e framework including educated guess on light yield and electronic noise with the final setup.

The measurement of the light yield has been performed using a modified version of the LNF QA station developed for determining the response and the longitudinal uniformity of the LYSO crystals. The station was modified by adding a UV extended PMT from EMI while the mechanics for the movement of the Na^{22} source was kept unchanged. The EMI photo tube has a QE $\sim$ 30% @ 220 nm and an operation gain of 3.8×10^6 for an high voltage set at V_{bias} = 1800 V. With this setup we measured the response of the BaF_2 to the source in two different wrapping conditions (Teflon foil and ESR 3M reflector) and by coupling the PMT to the crystal in air, i.e. without the application of any optical grease. Figures 6 shows the integated charge in a time window of 50 ns (left) and of 650 ns (right) respectively. The shorter time window has been selected to give a first estimate of the expected prompt component due to the total signal width of the PMT and of the RMD APD's (that is expected to be $\sim$ 40-50 ns).

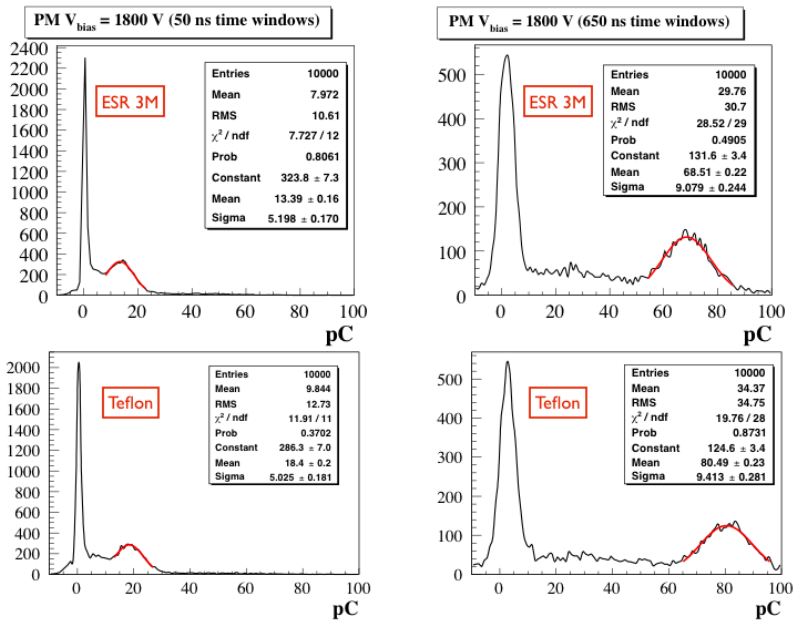

Figure 6. Left: integrated chrge distribution in 50 ns time window. Right: integrated charge distribtuion in 650 ns.

The best light output result was obtained with the Teflon wrapping. In this configuration the measured light yield, in 50 ns integration window, is 15.0$\pm$3.8 pe/MeV. Scaling this result to the expected area and quantum efficiency of the RMD APD, and applying a factor of two correction

for the usage of optical grease or glue, we expect the light yield to be of ~ 30 pe/MeV. A dedicated measurement of the light yield obtained with the first RMD prototypes will be carried out during next autumn.

We have also estimated the expected electronic noise (in MeV) for the BaF_2 crystal starting from the measurement done for the LYSO crystals and related FEE electronics. The electronics, see figures 7 and 8, consists of a discrete preamplifier chip and a local HV regulator that has been developed by the LNF electronic departments to grant an amplification of G$\sim$ 300, a precise stability on voltage supply and a ENC of 1000 e^- without input source connected. For the LYSO case readout by a S8664 APD from Hamamatsu, that has a capacitance of 270 pF, we have measured an ENC of 13000 e^- at an APD gain of 150. This noise corresponds to a ENE of 30 keV. For the BaF_2 case, the RMD APD has two improved characteristics with respect to the S8664: (i) a capacitance of 60 pF and (ii) an operation gain of 500. The ENC(e^-) will be of $\sim$ 5000 e^-. Assuming a light yield of 30 pe/MeV, the expected noise level is ENE=ENC(e^-)/(G $\times$ LY) = 5000/(30 $\times$ 500) = 0.33 MeV.

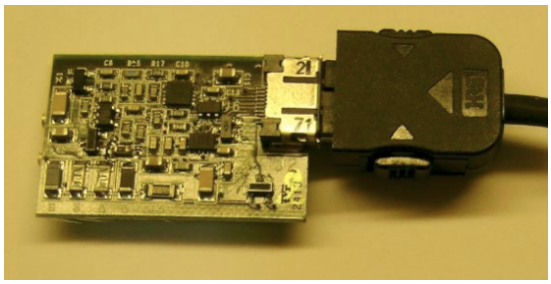

Figure 7. Amp-HV prototype.

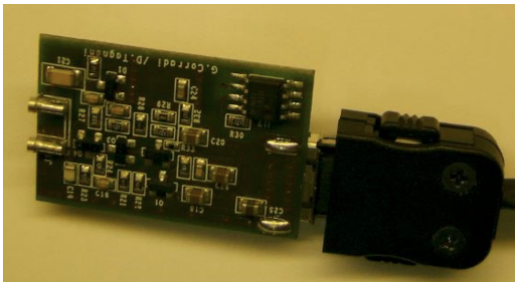

Figure 8. Amplification HV side.

We have then simulated the calorimeter performance for reconstructing CE events by including the final optimized geometry, all the environmental background surces in the experiment (photon, protons and neutrons from muon capture and related secondaries, DIO events) and the estimated values of the light yield and of the electronic noise. To be realistic and in order to test the dependence of the resolution to these experimental inputs we have varied them up to a factor of two.

Figure 9 shows the distribution of the energy residuals. The 20 cm ($\sim 10\ X_0$) length of the BaF_2 crystal does not allow the total containment of the electron shower, which results in the long tail on the right of the distribution. The value of the FWHM/2.35 of the distribution is $\sim$ 4.3 MeV. For testing the stability of the energy resolution several simulations (with and without the background mixed) have been performed including the electronic noise contribution and assuming different photo detection efficiencies. Figure 10 shows that scaling to $\sim$ 20 p.e./MeV the expected FWHM/2.35 is less than 5 MeV.

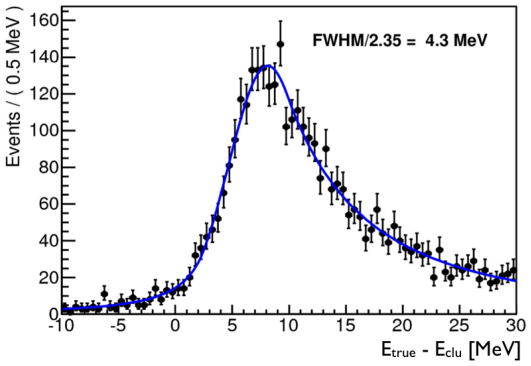

Figure 9. Distribution of the difference between the energy at the entrance of the EMC (E_{true}) and the energy deposited in the EMC (E_{clu}). The blue line is the result of the fit with a "Crystal-ball" function [9] able to describe the asymmetry due the non-perfect energy containment.

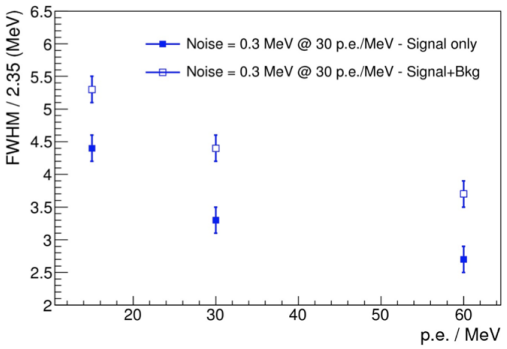

Figure 10. Dependence of the energy resolution for a BaF_2 based calorimeter as a function of the light yield for different values of electronic noise, and with and without nominal background..

3.6. Absolute calibration and system monitoring

The absolute energy scale, the equalization in response of the crystal, as well as a check of response linearity are provided by a liquid source system (C_8F_{18}) which is pumped through aluminum pipes (3 mm of diameter) which cover both disk surfaces. This liquid source can be activated by a neutron source, producing the following decay chain:

$$\begin{aligned} {}^{19}F + n &\rightarrow {}^{16}N + \alpha \\ {}^{16}N &\rightarrow {}^{16}O^* + \beta^- + \bar{\nu}_e \ (\tau_{1/2} = 7\text{s}) \\ {}^{16}O^* &\rightarrow {}^{16}O + \gamma(6.13 \text{ MeV}) \end{aligned}$$

The fluorine activated by the neutron source produces the ^{16}N isotope, which decays with an half-life time of 7 s in to an exited state of the ^{16}O, which finally decays to its ground state emitting a 6.13 MeV photon. The source spectrum, as seen with a CsI(Tl) crystal [6] with PIN diode readout is shown in figure 12. There are three principal contributions to the overall peak, one at 6.13 MeV, another at 5.62 MeV, and the third at 5.11 MeV, the latter two representing escape peaks. It is important to note that all three peaks have well-defined energies and thus all are useful in the calibration, providing both an absolute calibration and a measurement of linearity. Figure 11 showes the liquid source circuit which is planned to be used. It is constitued of 12 Al pipes, 0.5 mm thick, with a diameter of 3/8 inches and a length which ranges from 1.5 to 1.7 m. The selected geometry allows to have an uniform illumination of the disk with variation on the intensity less then 5%.

The variation of the crystal optical transmittance and photosensors' gains will be monitored in a continuos way by means of a laser system, following a scheme similar to the one used for CMS [7]. To achieve this goal, each crystal is illuminated by UV light transported it, with fused silica optical fibers, to the back of each BaF_2 crystal. A reference monitor station based on Pin Diodes will also be used to control the variation of the input laser source and of the fibers at the end of the distribution system. In Figure 13 the basic scheme of the laser system in Mu2e is shown. Prototype of the distribution system has been developed and tested in preparation for the upcoming test beam periods.

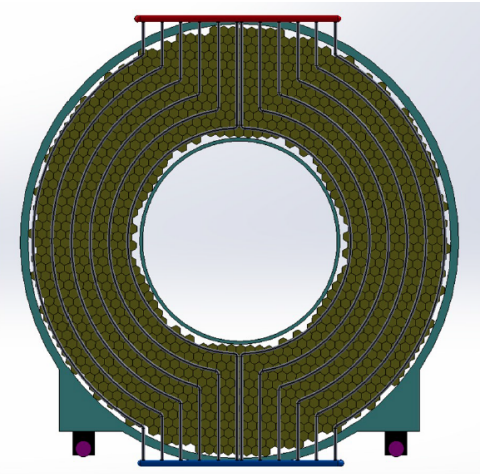

Figure 11. Liquid source circuit scheme.

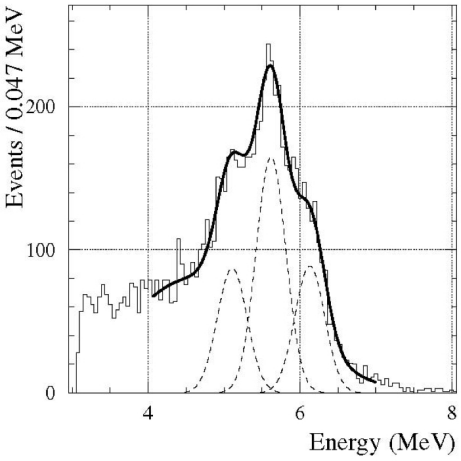

Figure 12. Energy spectrum in a *BABAR* CsI(Tl) crystal irradiated with 6.13 MeV photons from an $^{16}O^{*}$ source. The solid curve is a fit to the data, including Gaussian contributions at 6.13 MeV, 5.62 MeV, and 5.11 MeV, indicated by the dashed curves.

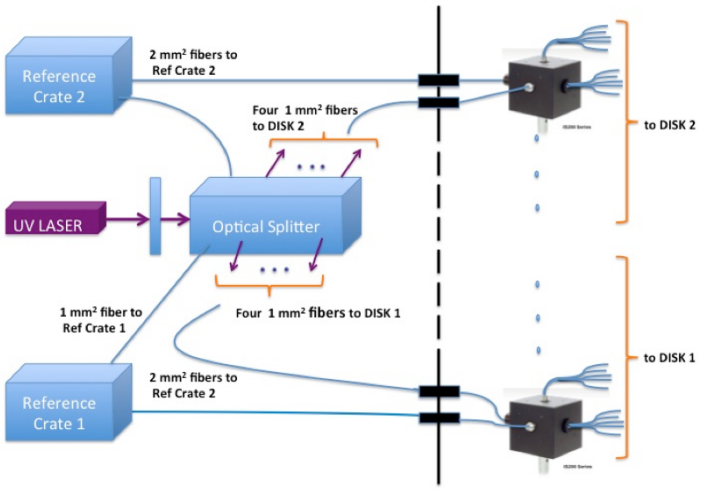

Figure 13. Laser system scheme.

In the final setup, one UV pulsed lasers will funnel light in a integrating sphere of 2" diameter through a dichroic prism outside of the DS.

3.7. Calorimeter driven pattern recognition

The first stage of the track reconstruction is the pattern recognition of the hits in the tracker. The straw tube has a diameter of 5 mm and the maximum drift time is $\sim$ 50 ns while a CE crosses all the detector region in $\sim$ 15 ns. Once a calorimeter cluster is identified as "candidate" (just looking at the deposited energy), its time can be used for collecting a pattern of hits in the tracker which are close in time with the calorimeter cluster in a window of $\sim$ 50 ns.

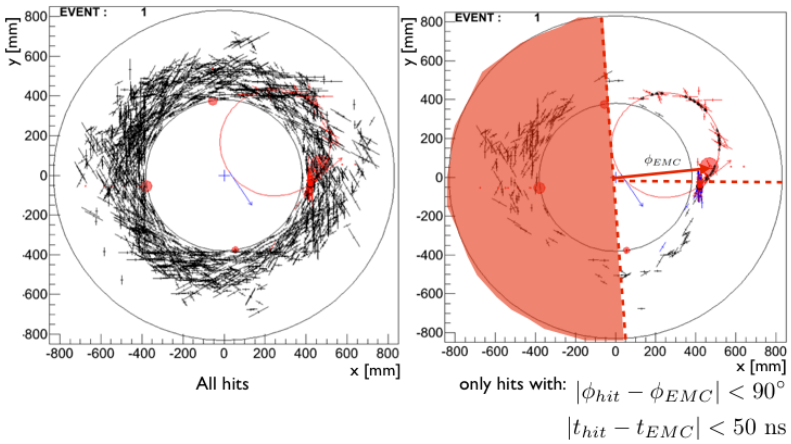

Figure 14. CE with background overlapped (left) and after time selection (right).

Moreover also the calorimeter cluster position allows to reduce significantly the tracker occupancy. Figure 14 shows that setting a cut on the angular distance between the straw hits (ϕ_{hit}) and the calorimeter cluster (ϕ_{EMC}) at 90° helps on reducing the tracker occupancy by a factor > 2. When simulating the CE with all background hits in overlap, the described procedure is able to increase the reconstruction efficiency by a factor $\sim 12\%$. Such a result improves when increasing the background rate.

3.8. Calorimeter particle identification

Rejection of background due to cosmic rays (CR) requires either the identification of muons mimicking the CE or the removal of electrons directly produced by CR. At low energies, a strong particle identification technique is based on the fact that at the same momentum, particles with different masses travel at different speed. In case of Mu2e signal, 100 MeV/c electrons could be considered ultra-relativistic ($E/m_e \sim 200$), while 100 MeV/c muons travel at a speed of about 0.7 c. Extrapolating the reconstructed track, it is possible to predict the particle arrival time and impact position on the calorimeter surface. Using the correct assumption about the particle mass, the predicted time will be close to the reconstructed time of the calorimeter cluster. All the way around, if a muon track has been extrapolated into the calorimeter assuming it was an electron, the predicted arrival time of the muon will be systematically lower than the reconstructed time of the calorimeter cluster associated to the track.

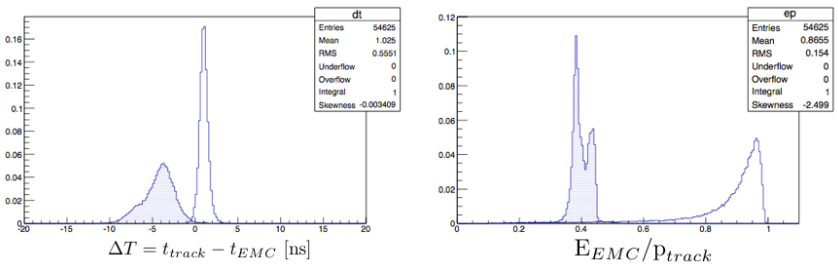

Figure 15. (Left) Distribution of $\Delta T = T_{track} - T_{cluster}$ [ns] for 100 MeV/c electrons (open histogram) and muons (blue filled histogram). (Right) Distribution of E / P for 100 MeV/c electrons (open histogram) and muons (blue filled histogram). E is the cluster energy from the calorimeter and P is the reconstructed momentum.

Figure 15 (left) shows the distributions in $\Delta T = T_{track} - T_{cluster}$ for 100 MeV/c electrons and muons; T_{track} is the predicted time of the particle at the calorimeter, calculated from the reconstructed track, and $T_{cluster}$ is the reconstructed cluster time. The separation between the maxima of the electron and muon distributions is $\sim$ 5 ns.

The distribution of the deposited energy in the calorimeter is also very different between electrons and muons. Figure 15 shows distributions in E/P, where E is the cluster energy and P is the associated track momentum. The kinetic energy of a 100 MeV/c muon is about 40 MeV. The structure and the tail above 50 MeV in the muon energy deposition are due to the capture and beta decay of the stopped muons, as modeled by Geant-4. A likelihood-based approach allows to reach an overall muon rejection factor of $\sim$ 500 (with an electron identification efficiency $\sim$ 99.9%), which is above the requirement of the experiment set at $\sim$ 200. The latter requirement is driven by the consideration that, when simulating a very large sample of Cosmic Ray, equivalent to the full elapsed time of the experiment, 11 muons were able to fake the CE signal in the tracker while were not vetoed by by the CRV system. Since the experiment wants to keep the CR related background contained to 0.05 event, a factor 200 of rejection is needed.

3.9. Calorimeter based trigger

So far, the developed calorimeter trigger algorithm is based on the application of an energy threshold on the reconstructed cluster energy. To study the efficiency and the performances of this method CE and DIO electrons were simulated with the Mu2e official framework [8]. DIO electrons were simulated since they represent the most intense source of background that can create calorimeter clusters. In order to study the behavior of trigger efficiency and DIO rejection on the calorimeter performances, we have convoluted the energy simulated by Geant-4 with additional Gaussian functions to deteriorate the resolution.

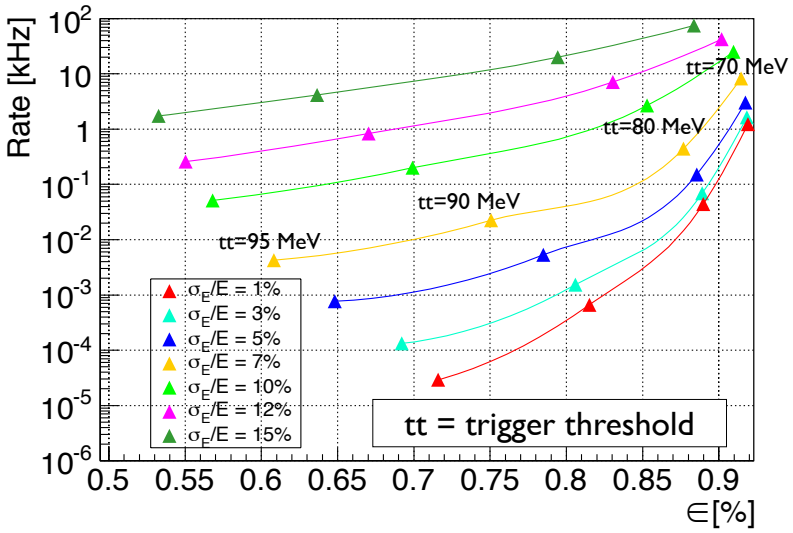

Figure 16. DIO's rate versus the signal efficiency. The different colors shows results from different assumptions on the energy resolution indicated relatively to 100 MeV.

Figure 16 shows the DIO's rate as a function of the signal efficiency for all the configurations tested. In the case of an energy resolution of $\sim$ 5%, it demonstrates that when setting a trigger

threhold at 70 MeV we can get a signal efficiency $\sim 92\%$ while reducing the DIO rate down to ~ 2 kHz.

3.10. Calorimeter dose

To evaluate the total dose absorbed by the calorimeter all the processes related to the muon beam arrival in the detector solenoid have been studied within the Mu2e framework:

- The beam flash. This component is constitued by all particles wich reach the DS practically in time with the μ beam (π 's, e^- 's, ecc);
- Electrons from μ decay-in-orbit (DIO) processes;
- μ out-of-target (OOT);
- All secondary products related to the μ nuclear capture: photons, neutrons, protons;

The calorimeter dose have been evaluated separetly for the two disks. For the first disk (the one closer to the target), in figure 17, we show the crystal dose as a function of the radial distance, evaluated with respect to the beam axis. The beam flash is the most relevant contribution for the ionization dose. The inner ring is the hottest region with ~ 15 krad/year. in the rest of the disk the dose/year is almost constant at a value of ~ 4 krad/year. To validate this result

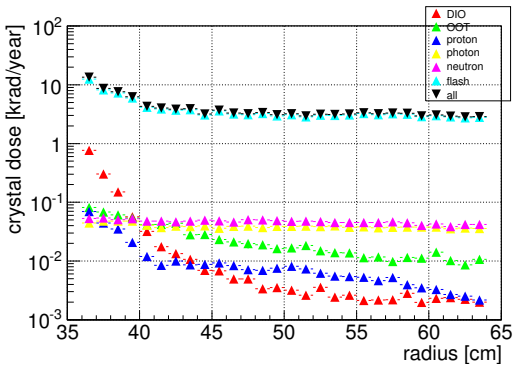

Figure 17. Disk 1: Crystal dose (krad/year) versus the radial distance (cm).

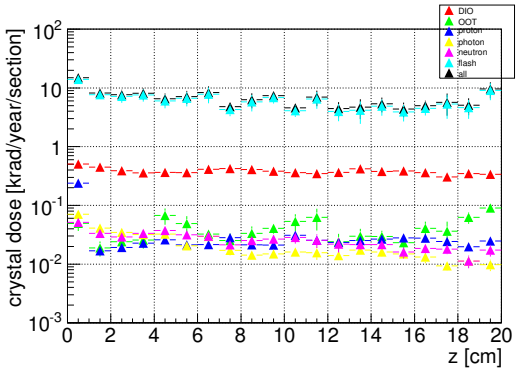

Figure 18. Disk 1: Crystal dose (krad/year/section) versus the crytal depth (cm).

also the dose along the crystal has been studied. Figure 18 shows the dose/year/section for the crystals in the inner ring of the first disk as a function of the crystal depth. It shows that

As one naively expects, the dose in the second disk is smaller, thanks to the shielding effect provided by the first one. Figure 19 shows the dose as a function of the radial distance. The hottest area, as in the previous case, is the inner ring, where the dose is ~ 8 krad/year, than the dose scales down at 0.2 krad/year for radial distances higer then 50 cm.

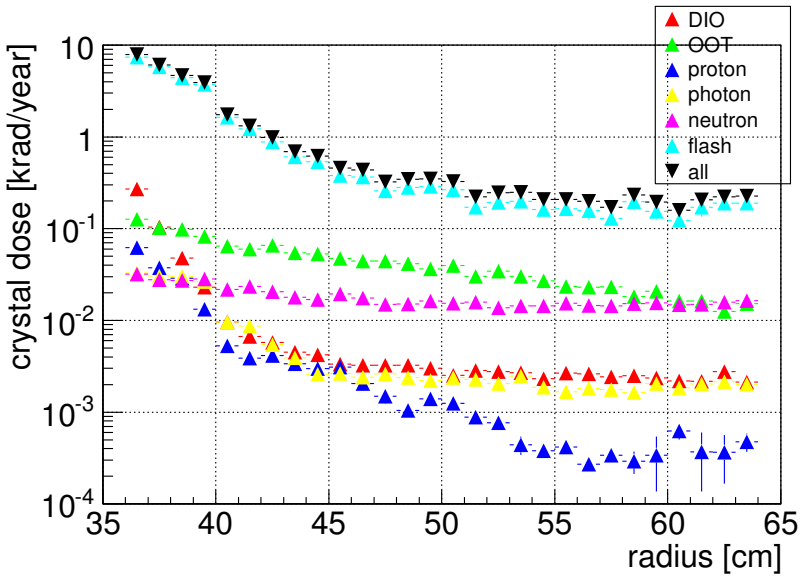

Figure 19. Disk 2: Crystal dose (krad/year) versus the radial distance (cm).

4. Conclusion

In this paper the calorimeter project for the Mu2e experiment has been presented. We have shown that the calorimeter design is able to satisfy the Mu2e requirements, providing excellent particle identification, an efficient trigger and is also a helpfull tool for improving the tracking pattern recognition. Simulation studies, integrated with eperimental measurements of light yield and electronic noise, indicated that we can achieve an energy resolution of O(5 MeV) at 100 MeV. Test beam with a small prototype of the calorimeter is under construction for validating the simulation results in this energy region.

References

[1] J. Adam et al, *New constraint on the existence of the* $\mu^+ \to e^+\gamma$ *decay. Phys. Rev. Lett.* 110 (2013), 201801 .
[2] W. Bertl et al, *A search for* $\mu - e$ *conversion in muonic gold. The European Physical Journal C - Particles and Fields 47(2) (2006), 337-346*.
[3] William J. Marciano et al, *Charged lepton flavor violation experiments. Annual Review of Nuclear and Particle Science* 58 (2008), 315-341.
[4] J. R. Abrams et al, *Mu2e conceptual design report*
[5] M. Cordelli et al, *Test and Simulation of a LYSO+APD matrix with a tagged Photon Beam from 40 to 300 MeV J. Phys.: Conf. Ser.* 404 (2012) 012027
[6] B. Aubert et al, *The BABAR detector. Nucl. Instr. Meth. A 479 (2002), 1*.
[7] M. Anfreville et al, *Laser monitoring system for the CMS lead tungstate crystal calorimeter. Nucl. Inst. Meth. A* 594 (2008), 292.
[8] Robert K. Kutschke, *Offline Software for the Mu2e Experiment J. Phys.: Conf. Ser.* 396 (2012), 022028
[9] T. Skwarnicki, *A study of the radiative cascade transitions between the* υ' *and the* υ *resonances. Ph.D Thesis*, DESY F31-86-02(1986) Appendix E